Advances in Materials Science and Engineering

WILEY

RESEARCH ARTICLE OPEN ACCESS

A Predictive Design Framework for Tunable Structural Colour Inspired by Morpho Nanostructures

Tobias Rosnitschek | Sara Al-Motori | Christian Orgeldinger | Markus Zimmermann | Stephan Tremmel

Engineering Design and CAD, University of Bayreuth, Universitätsstr. 30, Bayreuth 95447, Germany

Correspondence: Tobias Rosnitschek (tobias.rosnitschek@uni-bayreuth.de)

Received: 5 December 2025 | **Revised:** 6 January 2026 | **Accepted:** 12 February 2026

Academic Editor: Mohammad Rezwan Habib

Keywords: biomimetic design | colour tuning | optical metamaterials | structural colours

ABSTRACT

Structural colour arises from light interacting with nanoscale architectures, yet generalizable design rules for engineering such effects remain limited. Here, we introduce a predictive design framework for tunable structural colour based on simplified Morpho-inspired photonic nanostructures. Using electromagnetic finite-element simulations, we systematically vary geometric parameters and derive a linear scaling law linking structural dimensions to reflection wavelength, enabling both forward colour prediction and inverse geometry estimation. Angle-resolved analyses reveal that reflectance is maximized at shallow incidence angles, offering insights for wide-angle optical functionality. To support practical design workflows, simulated spectra are mapped into RGB colour space for intuitive visualization. This framework provides an efficient route to engineer bioinspired photonic surfaces with tunable colour responses, relevant for coatings, sensors, and optical materials.

1 | Introduction

Structural colour arises from the interaction of light with nanoscale architectures that modulate reflection, scattering, and interference. Unlike pigments, which rely on molecular absorption, structural colours emerge from geometry-dependent photonic effects and offer tunability and angular responsiveness that are valuable for engineering optical materials. Natural systems such as butterflies, beetles, and birds demonstrate how nanoscale geometries can produce vibrant, stable colours, inspiring research on bioinspired photonic surfaces for coatings, sensing, and energy applications. The photonic mechanisms underlying the iridescent blue of *Morpho* butterflies (see Figure 1) have been extensively characterized experimentally and numerically [1]. Seminal work has shown how alternating lamellae, tapered ridge geometries, and height disorder collectively generate wide-angle reflection in the 450–500-nm range [2, 3]. While these studies provide outstanding biological insight, translating such complex, species-specific architectures into generalizable design rules for engineered materials with approximation of the resulting structural colour remains challenging. Existing work largely focuses on biological fidelity; far fewer studies examine how such effects persist, or transform, when transferred onto arbitrary artificial materials used in photonic engineering.

At the same time, advances in electromagnetic simulation enable systematic, geometry-driven exploration of photonic structures before fabrication. Finite-element modelling is particularly well suited for studying complex, heterogeneous geometries, making it a powerful tool for deriving quantitative relationships between structural geometry and optical response. By designing surfaces at the nanoscale, optical metamaterials enable novel applications in photonics, telecommunications, and sensing technologies, while recent advances in additive manufacturing have expanded the possibilities for fabricating microstructured materials with unprecedented precision [4]. These developments create a timely opportunity to translate biological inspiration into generalizable and fabrication-ready design rules for engineered photonic systems. Recent advances in photonic crystals and bioinspired

---

https://doi.org/10.1155/amse/9921260

FIGURE 1 | Picture of the *Morpho didius* butterfly.

architectures further underscore the rapid evolution of structural-colour engineering beyond the biology-related motifs. Emerging strategies increasingly leverage three-dimensional periodicity, hierarchical architectures, and programmable photonic concepts to realize scalable and multifunctional optical responses, including controlled angular behaviour, stimulus-responsive colour tuning, and coupled optical–thermal functionality [5–7]. At the same time, progress in engineered photonic surfaces highlights that practical deployment often hinges on design rules that remain robust under material substitution and fabrication tolerances, particularly when transferring optical functions from natural prototypes to technologically relevant substrates [8]. Building on bio-inspired archetypes, this work aims to translate structural colour concepts into a computational and engineering-oriented framework aimed at predictive design rather than biological reproduction. Within this landscape, there remains a complementary need for low-dimensional, geometry-driven frameworks that enable rapid forward prediction and inverse targeting of colour without requiring full architectural redesign. Such frameworks can serve as efficient "pre-design" layers for more complex photonic crystal concepts, providing fast, interpretable guidance for choosing geometric scales and target wavelengths before detailed three-dimensional optimization.

1.1 | Objective of This Work

In this study, we develop a predictive computational framework for tunable structural colour based on simplified morpho-inspired nanostructures. Rather than attempting to replicate biological systems, we deliberately work with the artificial material silicon carbide (SiC). This choice is central to our objective to evaluate whether structural colour effects persist across materials and to assess the extent to which geometry, not material composition, dominates the spectral behaviour. By comparing reflectance trends obtained with SiC to known biological results, we demonstrate the material-agnostic nature of the underlying geometric mechanisms, highlighting the primacy of surface structure colour formation. Using electromagnetic FEM, we systematically vary structural dimensions to derive a linear scaling law linking geometry to reflection wavelength, enabling both forward colour prediction and inverse geometry estimation. Angle-resolved simulations show that reflectance maxima consistently occur at shallow incidence angles, reinforcing wide-angle design principles observed in biological systems. To support engineering workflows, simulated spectra are mapped into RGB colour space for intuitive visualization.

1.2 | Optical Metamaterials

Optical metamaterials are engineered structures that enable precise control over permittivity and permeability, including the realization of negative refractive indices and associated phenomena such as reversed refraction and sub-diffraction imaging [9, 10]. These properties arise from nanoscale patterning rather than chemical composition and have unlocked applications in super-resolution optics, cloaking, and photonic devices [11]. Dielectrics, semiconductors, and metals play essential roles in this context, as their nanoscale optical behaviour, especially scattering, dispersion, and plasmonic resonances, strongly influences effective medium responses [12, 13]. Metal–dielectric composites, in particular, can be described using classical and extended mixing rules that relate constituent parameters to emergent optical properties. Because analytical treatments are limited for complex, heterogeneous geometries, numerical methods have become indispensable for predicting light–matter interactions in metamaterials. They provide the foundation for modelling bioinspired photonic architectures and for extracting generalizable design principles applicable across materials.

1.3 | Biomimetic Approaches for Optical Metamaterials

Biological systems provide diverse strategies for manipulating light through nanoscale structuring, offering valuable templates for engineered optical metamaterials. Organisms such as butterflies, beetles, birds, reptiles, and chameleons generate vivid colouration through interference, diffraction, scattering, or combinations thereof, demonstrating how geometry can be used to tune optical responses. Chameleons such as *Furcifer pardalis* exemplify dynamic colour control: reversible reconfiguration of guanine nanocrystal lattices within iridophores modulates reflected wavelengths from blue-green to yellow-red, illustrating a biologically optimized, tunable photonic crystal system [14]. In contrast, many birds employ quasi-ordered β-keratin/air nanostructures that generate non-iridescent colours through locally correlated scattering [15]. Three-dimensional electron tomography has shown that these spongy architectures form bicontinuous networks with short-range order in all directions, enabling coherent scattering and accurate spectral prediction through 3D Fourier analysis [16]. Such systems highlight how structural and pigmentary colouration often coexist and interact, producing hybrid optical responses in birds and butterflies [17].

Beetles provide additional insight into thin-film interference mechanisms. Coleoptera display a broad range of iridescence modes—from multilayer reflectors to photonic crystals and diffraction gratings [18, 19]. In *Chrysochroa fulgidissima*, only a few superficial multilayers dominate the optical response, finely adjusting phase relations to enhance constructive interference at the air–cuticle interface [20]. These studies demonstrate how relatively simple layered structures achieve angle-dependent reflectance suitable for signalling, camouflage, or predator avoidance [19].

Structural colouration in *Morpho* butterflies has been extensively investigated due to its vivid blue appearance and robust angle-insensitive response. Alternating lamellae, tapered ridge geometries, and height disorder collectively contribute to broad reflection bands (≈60–90 nm) and wide-angle iridescence [21, 22]. In the context of this work, broad reflection bands refer to a reflectance peak that spans a comparatively wide wavelength interval—here about tens of nanometres—rather than a narrow resonance. In morpho-type architectures, such band broadening arises from the stacked lamellae within each ridge, where multiple closely spaced interfaces contribute interference conditions. Subsequent research revealed additional functional architectures: quasi-ordered tubular–gyroid networks in *Morpho theseus* generate broadband structural whiteness and support thermoregulation [13], while SiC-based ridge structures have been used to enhance near-field radiative transfer in the 8–13 μm atmospheric window through NF-RT-FDTD analysis [21]. These examples illustrate the versatility of structural colour systems, which integrate interference, scattering, and diffraction effects beyond what pigment alone can achieve [2], and demonstrate how bioinspired principles can interface with scalable optical technologies such as LED-based spectrophotometry [18]. Collectively, these natural photonic strategies showcase the broad design space accessible through nanoscale structuring and motivate the development of computational frameworks capable of predicting and tuning optical responses in engineered materials.

1.4 | Numerical Simulation of Optical Metamaterials

Numerical simulations are central to the analysis and design of optical metamaterials, as their subwavelength geometries and heterogeneous compositions often preclude analytical solutions. Computational methods based on Maxwell's equations provide accurate predictions of scattering, interference, and near-field effects essential for structural colour analysis [12]. Among these approaches, the finite element method (FEM) is especially suited for modelling complex, bioinspired nanostructures. FEM supports flexible meshing, accurate treatment of material dispersion, and the incorporation of boundary conditions such as periodicity and perfectly matched layers (PMLs). It has therefore been widely applied to study photonic structures derived from butterfly wings, beetle cuticles, and bird feathers [21]. In this work, FEM is used to compute reflectance spectra and electromagnetic field distributions of simplified morpho-inspired geometries. A typical simulation workflow involves constructing the geometric model, generating a mesh, assigning complex refractive indices to each material region, and applying appropriate boundary conditions. Solving the resulting system yields spatial and spectral electromagnetic fields. Parametric sweeps over structural variables enable systematic exploration of design dependencies, supporting both forward prediction and inverse design of optical functionalities such as broadband reflection, narrowband absorption, or angular robustness [1, 21].

2 | Materials and Methods

The simulations in this work were carried out in COMSOL Multiphysics 6.3, following the software's native notation to ensure transferability. The complete simulation model, including geometry, material definitions, and solver settings, is openly available on Zenodo [23] to support reproducibility and FAIR data practices. The modelling approach adopted in this work is deliberately design-oriented rather than biologically exhaustive. While prior studies of morpho-inspired, for instance, [1, 13] or [21], structural colour have focused on high-fidelity reconstruction of wing scale morphology to elucidate biological mechanisms, the present work aims to extract a transferable and computationally efficient relationship between geometry and optical response. Accordingly, we employ a simplified ridge–lamella motif derived from established microscopy-based models and combine it with systematically varied geometric scaling to identify first-order design rules for structural colour tuning. This abstraction allows us to decouple geometric effects from material-specific details and to evaluate colour transferability across material platforms without introducing additional architectural complexity. While silicon carbide (SiC) was selected here as a technically robust reference material, due to the availability of optical constants and its relevance for engineering photonic systems, the presented framework is not tied to this material choice. From a biomimetic and sustainability-oriented perspective, it is important to note that natural structural colours are realized in bio-based materials such as chitin, keratin, or cellulose, which exhibit lower absorption and additional functionalities including biodegradability and biocompatibility. A systematic exploration of bio-derived materials is therefore a natural extension of this work.

2.1 | Modelling Environment

Finite-element simulations were performed using COMSOL's frequency-domain electromagnetic module, which allows accurate modelling of subwavelength nanostructures and evaluation of their spectral response. Parametric sweeps and geometric scaling were implemented to identify relationships between structure size and reflected wavelength.

2.2 | Nanostructure Design

The nanostructure model was designed to emulate the multilamellar ridge architecture found on the scales of *Morpho didius* wings, based on the geometrical parameters reported by Didari and Mengüç [21]. A simplified structure consisting of 13 lamellae (seven on one side, six on the other), each 65 nm in height, was constructed using parametric definitions to enable systematic scaling. A central supporting rod was included, and the entire structure was merged into a single volumetric domain (Figure 2(a)).

2.3 | Geometrical Boundary Conditions

To emulate an infinite or periodically repeating photonic structure, the computational domain was enclosed within PMLs above and below the structure, designed with polynomial coordinate stretching (1 μm in x, 0.3 μm in y) to absorb outgoing waves. Further, we applied Floquet–periodic boundary conditions (PBCs) on the lateral boundaries to impose lateral periodicity and define the in-plane wave vector via a periodic port. An air domain surrounding the nanostructure ensured physically meaningful boundary interaction. All geometrical domains were unified prior to meshing. Boundary-condition parameters are summarized in Table 1 and visualized in Figure 2(b).

2.4 | Material Properties

The structural material used was silicon carbide (SiC), more precisely 6H-SiC, a polytype of silicon carbide known for its high refractive index, thermal stability, and good IR transparency. The optical properties were defined using values from Didari and Mengüç [21], Siddique et al., and Feng et al. [1, 24], while in

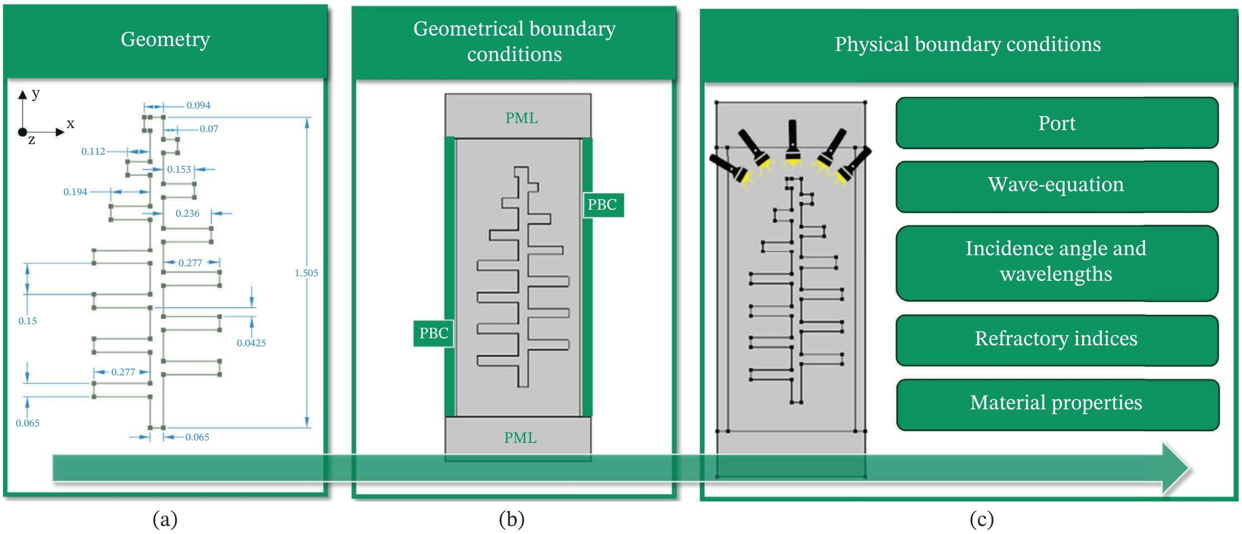

(a) (b) (c)

FIGURE 2 | Simulation setup: (a) geometry of the wing's nanostructure in μm; (b) geometrical boundary conditions; (c) physical boundary conditions.

TABLE 1 | Geometrical boundary conditions as defined in the COMSOL model.

PML–geometry	
Type	User-defined
Number of stretching directions and thickness	2 direction 1: x-direction (1 μm) direction 2: y-direction (0.3 μm)
PML–scalability	
Coordinate extension type	polynomial
PML scaling factor (curvature parameter)	1
PBC–periodicity settings	
periodicity-type	Floquet- periodicity
k-vector for Floquet periodicity	From the periodic port

general, reliable wavelength-resolved optical constants for bio-based materials remain sparse, representing a current bottleneck for quantitative structural colour simulations. The refractive index, relative permittivity, and relative permeability are given in Table 2. The permittivity in the nanostructure was calculated from the complex refractive index.

The surrounding medium, including PML and PBC regions, was modelled as air with $n_r = 1$ and $n_i = 0$.

2.5 | Electromagnetic Wave Propagation

In the following, electromagnetic wave propagation is described using standard material parameters commonly employed in computational photonics. The real part of the refractive index determines the phase velocity of light within a material, while the imaginary part accounts for absorption losses, which reduce reflectance intensity. The relative permittivity ε describes how strongly a material polarizes in response to an electric field and directly governs interference and resonance effects in nanostructures. Frequency-dependent models, such as the Drude–Lorentz formulation, are used to capture dispersive behaviour in a physically consistent manner. Solving the frequency-domain Maxwell equations yields spatial field distributions and wavelength-dependent reflectance spectra, which form the basis for the colour analysis presented in this work. The governing physics were defined using the frequency-domain electromagnetic wave equation [25–28]. Two separate domains were assigned different permittivity models: (i) the Drude–Lorentz model [29] for the air domain,

$$\varepsilon_r = \varepsilon_\infty + \sum_{i=1} \frac{f_i \omega_p^2}{\omega_{0_i}^2 - \omega^2 + i\Gamma_i \omega}, \tag{1}$$

and (ii) a refractive index–based formulation for the nanostructure.

$$\varepsilon_r = (n - ik)^2;\ \sigma = 0;\ \mu_r = 1. \tag{2}$$

The Drude–Lorentz parameters used are listed in Table 3.

The incident electromagnetic wave was linearly polarized along the z-direction, with the electric field vector.

$$\vec{E} = E \times \begin{bmatrix} 0 \\ 0 \\ 1 \end{bmatrix}. \tag{3}$$

TABLE 2 | Used material properties for SiC based on [1, 21, 24].

Property	Parameter	Value
Refractive index, real part	n_r	1.55
Refractive index, imaginary part	n_i	0.6
Relative permittivity	ε_r	9.7
Relative permeability	μ_r	6.7

Differences in permittivity across domains led to localized variations in the electric displacement field. A linearly polarized incident field was chosen to reduce computational complexity and to isolate geometry-driven interference effects. While natural illumination is typically unpolarized, the reflectance of periodic lamellar structures is well captured by single-polarization simulations, and the resulting spectral peak positions are not expected to shift under polarization averaging. Here, throughout the study, one polarization is used consistently to maintain comparability across parametric sweeps. Importantly, the peak position trends underpinning the scaling law arise from interference conditions of the geometry and are therefore expected to be robust, while polarization mainly affects relative intensities. The inclusion of polarization averaging is subject to future extensions.

In the frequency-domain wave optics formulation, the FEM solver returns the complex electric field distribution $E(r, \lambda)$ throughout the computational domain for each wavelength and incidence setting. Reflectance is not inferred qualitatively from field plots; instead, it is computed from port-based power quantities. In COMSOL, ports are internally normalized and can be used to evaluate reflectance and transmittance variables associated with each port. The wavelength-dependent reflectance spectra reported in this work were obtained by taking the ratio between the reflected power at the illuminated port and the prescribed input power. The effective colour is then derived from this ratio by mapping the dominant reflectance peaks into RGB space (see Section 2.9). Thus, the effective colour is determined by the spectral distribution of reflected intensity, not by the absolute magnitude of the local field.

2.6 | Ports and Excitation

To model illumination and extraction of electromagnetic waves, ports were implemented on the upper and lower surfaces of the simulation cell to introduce and extract electromagnetic waves. Port 1 (top) was defined as the source with wave excitation enabled, introducing a plane wave into the nanostructured region, while Port 2 (bottom) acted as an outlet with no excitation allowing transmitted and reflected fields to exit the domain without artificial reflections. Both ports employed periodicity and shared identical polarization characteristics. For each port, two diffraction orders were defined ($m = \pm 1$) with in-plane vector components and a mode phase. The slit condition was set to domain-supported, ensuring that diffraction orders are evaluated consistently within the computational domain, and port orientation was adjusted so that the energy flow was correctly directed through the structure. The initial incident angle was defined as $\alpha = 70°$, with an input line power of 1 W/m, to normalize the computed reflectance. All settings for the ports are summarized in Table 4, and the physical boundary conditions in total are shown in Figure 2(c).

2.7 | Mesh Generation

A physics-controlled mesh was employed, while the mesh resolution was adapted based on the smallest wavelength in the optical range (400–700 nm) to ensure adequate spatial resolution. The maximum element size was determined from the wavelength study settings.

2.8 | Study Configuration

The optical response of the nanostructure was evaluated in the frequency domain by sweeping the incident angle across the visible spectrum ranging from 400 to 700 nm, divided into 30 equidistant values to provide sufficient resolution for identifying reflectance maxima and overall spectral trends while maintaining computational efficiency. The incidence angle is imposed via the Floquet periodic excitation and referenced to the surface normal. A parametric sweep of the angle of incidence was also conducted to assess angular effects, with a starting point at 0°, a step length about 4.5°, and endpoint at 90°. This allowed for an accurate analysis of reflection and transmission behaviour across visible wavelengths and incident angles. Also, the baseline structure was scaled uniformly with scaling factors between 0.8 and 1.3 in order to analyse the sizing effect on the reflectance, the value of the scaling factor is denoted inside the ridge sketches in the results for better transparency. This geometric scaling study forms the basis for establishing the relationship between structural dimension and the resulting spectral position of the reflectance peak.

2.9 | RGB Mapping

To support intuitive visualization, reflectance spectra were mapped into RGB colour space using an empirical wavelength-to-RGB method derived from Bruton [30, 31]. While not a standardized colourimetric model (e.g., CIE 1931), it provides a perceptually meaningful approximation for the visible

TABLE 3 | Parameter for the Drude–Lorentz equation [21]; the notation from COMSOL Multiphysics is used for the parameters.

Parameter	Value
Frequency	From solver
Temperature	Global model setting
Relative permittivity ε_∞	6.7 (isotrop)
Plasma frequency ω_p/resonance frequency ω_0	$1.6512 \cdot 10^{14}$ (rad)/s
Damping constant Γ	$8.966 \cdot 10^{11}$ (rad)/s
Material equation	Relative permeability ($\mu_r = 1$/isotrop)

TABLE 4 | Settings for Port 1 and Port 2.

Parameter	Value
Incidence angle α	70°
Refractive index, real part n	1 (isotrop)
Maximum frequency	From study
Mode phase θ_{in}	0°
Input power P_{in}	$1\ W/m$

spectrum (380–720 nm). The conversion algorithm uses a piecewise mapping of wavelength intervals to RGB channels, with final intensities scaled near the spectral limits. The used algorithm, which represents an empirical mapping routine that converts wavelength-resolved reflectance information into approximate RGB values, is shown in pseudocode form in Figure 3. The result is a HEX-based colour representation displayed as a filled rectangle. To estimate an effective perceived colour for each geometry, we combine the three highest reflectance maxima in an overlay, using their intensity as transparency weights (Figure 4).

This functionality allows us to visualize the simulation results in a standard colour format and contributes to better understand the underlying phenomena. The inverse function (Figure 5) determines the closest matching wavelength for a given HEX code by minimizing Euclidean colour distance across the 401 discrete wavelengths in the 380–720 nm range. This brute-force approach is efficient and sufficiently accurate for our visualization purposes.

3 | Results and Discussion

3.1 | Reflectance Spectra

The initial morpho-inspired nanostructure (Figure 2(a)) exhibits a reflectance peak at 503 nm, corresponding to a turquoise-green hue, with a maximum intensity of 0.33 (Figure 6). This peak arises at a shallow incidence angle of approximately 4.5°, rather than at normal incidence, indicating a preferred angular offset for constructive interference. This behaviour is consistent with the previously reported morpho-type photonic structures, where near-perpendicular illumination maximizes coherent backscattering [1].

Across all simulated angles (Figure 7), reflectance systematically increases as the incidence angle decreases; however, that while most reflectance maxima are associated with small angles, they do not occur at normal incidence (0°). Instead, the dominant peak is consistently observed at an incidence angle of approximately 4.5°, indicating a preferential angular offset for maximum reflectivity. Wavelengths in the 430–490-nm region, corresponding to the blue-green area of the visible light spectrum, show the highest intensities for the unscaled geometry, confirming the inherent dominance of lamellar ridge architectures.

3.2 | Spectral Tuning by Geometric Downscaling

To access the blue spectral region between 450 and 490 nm, the structure was uniformly scaled by 0.94. This resulted in a clear blue shift, yielding a reflectance peak at 482.72 nm with a maximum intensity of 0.6, nearly twice that of the original configuration (Figure 8). A secondary maximum at 472.41 nm further reinforces the blue dominance.

Angle-resolved results show reduced spectral bandwidth but greater colour stability, implying that structural downscaling improves angular robustness of blue colouration which is consistent with the subwavelength nature of the lamellae.

3.3 | Spectral Tuning by Geometric Upscaling

Upscaling the structure by 1.08 yields a broadened spectral profile, with a global maximum in the green and local maxima extending into yellow and orange, indicating increased colour diversity (Figure 9). At 1.12 scaling, the primary reflectance peak shifts to 598 nm (orange), and the high-reflectance region narrows, demonstrating selective enhancement of longer wavelengths. The maximum reflectance increases by 0.142, highlighting that scaling modifies both spectral position and intensity.

Together, these results show that uniform structural scaling provides a direct and controllable mechanism for tuning the dominant reflected colour across the visible spectrum.

3.4 | Switching Colours and Establishing a Predictive Scaling Law

3.4.1 | Comparison With Established Morpho Models

The present simulation framework was benchmarked against experimentally validated morpho-inspired studies, most notably the work of Siddique et al. [1], which reports a blue reflectance maximum near 430 nm for PMMA-based Morpho structures. The ridge-lamella geometry used in this work closely follows the simplified structural description by Didari and Mengüç [21]; hence, differences in optical response can be attributed primarily to differences in refractive index, absorption, and dispersion between PMMA and SiC and modelling assumptions rather than to geometric inconsistencies. For the unscaled structure, our SiC-based simulations yield a dominant reflectance peak at 503 nm, corresponding to a turquoise-green hue and representing a deviation of approximately 14% from the PMMA-based experimental results reported in [1]. This spectral offset is expected and can be explained by two principal factors. First, silicon carbide exhibits a higher refractive index and absorption than PMMA in the visible range, which directly alters the effective optical path length within the lamellar stack. Second, the numerical model employs PBCs to represent an infinite array of ridges, whereas the experimental system consists of finite, multilamellar structures with intrinsic disorder and inter-ridge coupling effects that are known to influence spectral broadening and peak position. Crucially, when the same structure is uniformly downscaled by 6%, the dominant peak shifts to 483 nm with a reflectance of 0.6, closely resembling the blue maximum reported in [1]. These results show that geometric rescaling alone can compensate for changes in material properties. In other words, by adjusting only the scale, not the structural motif, it is possible to recover similar colour responses across different material platforms. This suggests a material-agnostic design strategy where structural colours can be transferred between materials by appropriate rescaling of the surface architecture rather than by redesigning the geometry. These findings indicate that small geometric tolerances on the

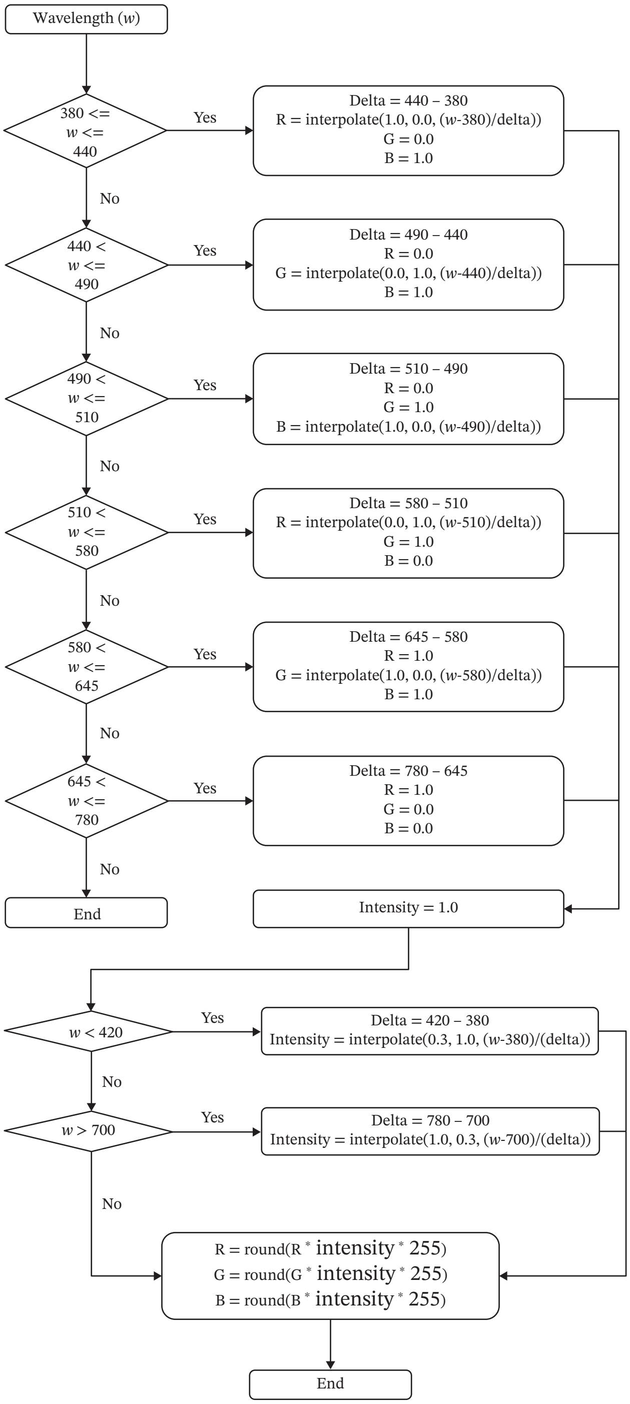

FIGURE 3 | Pseudocode description of the used wavelength to HEX code algorithm.

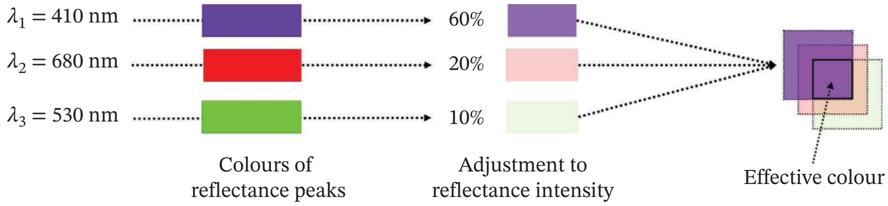

FIGURE 4 | Workflow for approximating the resulting colour from the obtained reflectance spectra.

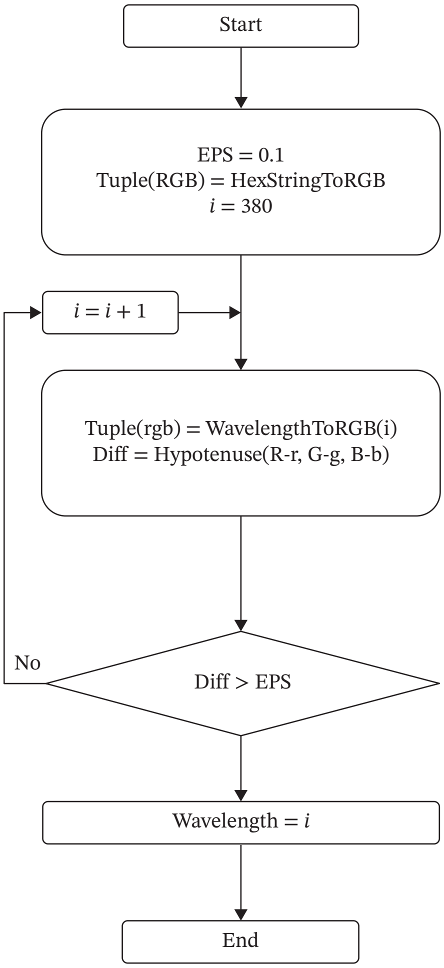

FIGURE 5 | Description of the function for identifying the "closest" wavelength for a given HEX colour code, using colour-distance minimization.

order of ±6% are sufficient to both achieve distinct colour transitions and reconcile differences arising from nonidentical optical constants. This is particularly relevant for biomimetic implementations, where fabrication constraints and material substitutions are common, yet target colours must remain consistent.

3.4.2 | Relationship Between Structural Scale and Reflected Wavelength

Throughout all simulations, a clear monotonic trend emerges, structures scaled by a factor $x \leq 1$ exhibit a systematic blue shift, while scaling with $x \geq 1$ induces a red shift in the reflected spectrum. Figure 10 quantifies this relationship by plotting the dominant peak wavelength (λ_{max}) and the effective colour wavelength (λ_{eff}) as functions of the scaling factor. Linear fits yield to $R^2 = 0.98$ and $R^2 = 0.95$, respectively, demonstrating that the reflectance peak varies approximately linearly with structural size in the explored range.

Thus, this first-order model enables a forward prediction—given a scaling factor, estimate the reflected wavelength—and inverse design—given a target wavelength (or colour), determine the required scaling factor. In combination with the material-agnostic behaviour discussed above, this scaling law provides a compact design rule for tuning structural colours across different materials by pure geometric rescaling. The predictive capability is further validated in Figure 11, where calculated colours based on λ_{max} and λ_{eff} are compared with colours extracted from *Morpho didius* wing images.

While the present study employs SiC as a representative engineering dielectric, the derived scaling relationship is fundamentally governed by geometric rescaling of optical path lengths within the lamellar motif rather than by material-specific chemistry. Uniform scaling modifies phase accumulation proportionally, thereby preserving the direction and approximate magnitude of the spectral shift across different material platforms. Material choice primarily affects the absolute reflectance amplitude and bandwidth through refractive-index contrast, absorption, and dispersion, whereas the position of the reflectance maximum remains dominated by geometry. Importantly, accurate wavelength-dependent optical constants for biological and polymeric materials, such as chitin or composite cuticular structures, are often incomplete, highly variable, or unavailable across the full visible spectrum, representing a persistent bottleneck in predictive structural-colour simulations. In this context, a geometry-driven scaling framework provides a practical alternative, allowing colour transfer and targeting without requiring exhaustive material characterization.

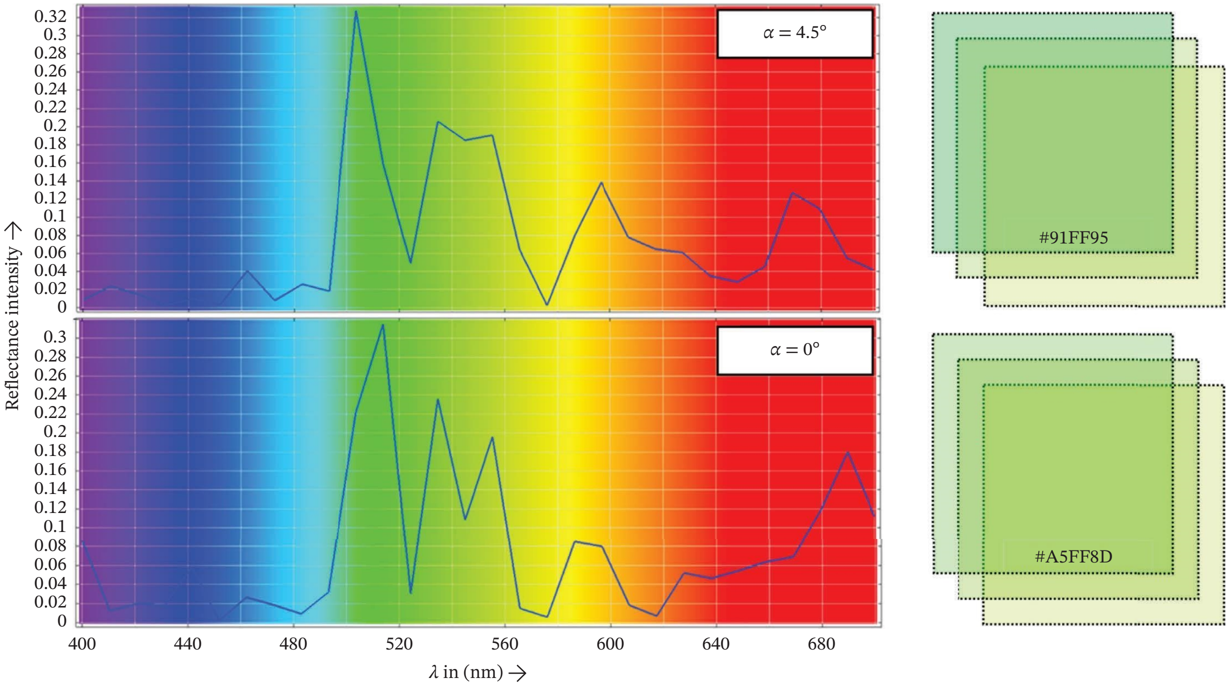

FIGURE 6 | Reflectance spectra of the structure shown in Figure 2(a) for the representative incidence angles with the highest reflectance intensity 0° and 4.5°. The reflectance is computed as normalized reflected power at the excited port. Each curve corresponds to a fixed angle of incidence measured relative to the surface normal. The coloured background indicates the visible spectrum for orientation only and does not determine the dominant perceived colour. The associated effective colours on the right were obtained as described in Figure 4.

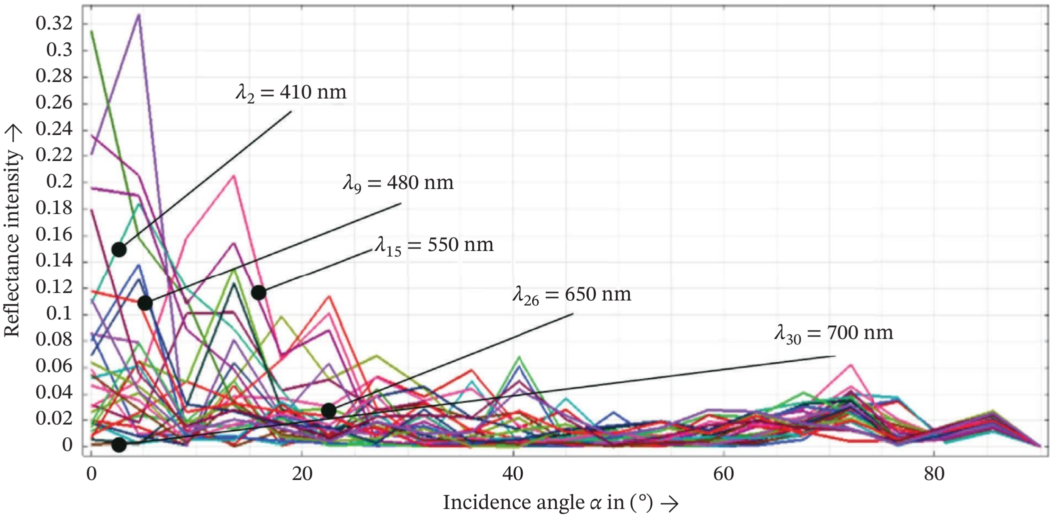

FIGURE 7 | Maximum reflectance as a function of the incidence angle for 30 wavelengths between 400 and 700 nm, where each curve corresponds to a fixed wavelength. The plot visualizes a general trend that colours among the “blue-area” between about 430 and 490 show the highest reflectance intensity for the initial structure presented in Figure 2(a).

3.4.3 | Mechanistic Interpretation

The observed colour tuning behaviour can be understood by considering how geometric scaling modifies the dominant optical interactions within the lamellar architecture. At shallow incidence angles, constructive interference between reflections from successive lamellae is maximized because the phase accumulation remains close to integer multiples of the wavelength. This explains why the strongest reflectance consistently occurs near small incidence angles and why angular dependence remains modest for blue-shifted configurations. As the structure is compressed or expanded, the optical path length between interfaces changes proportionally, producing predictable blue or red shifts in accordance with classical thin-film interference theory. Shorter wavelengths interact more strongly with the subwavelength features of the ridge structure. This enhanced interaction resembles a Rayleigh-like scattering contribution, in which the electromagnetic response increases rapidly as the

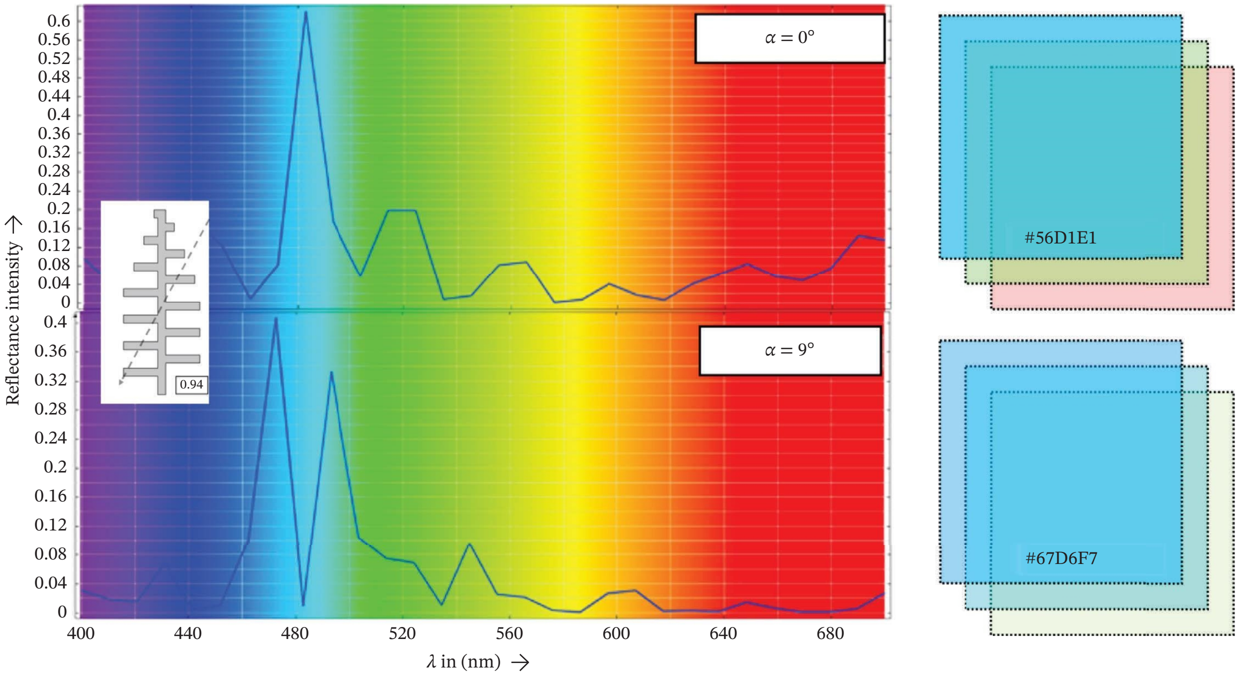

FIGURE 8 | Reflectance spectra associated effective colours for incidence angles with the highest reflectance intensity 0° and 9° of the down-scaled structure. The displayed scaling factor of 0.94 indicates a uniform geometric scaling of the baseline geometry.

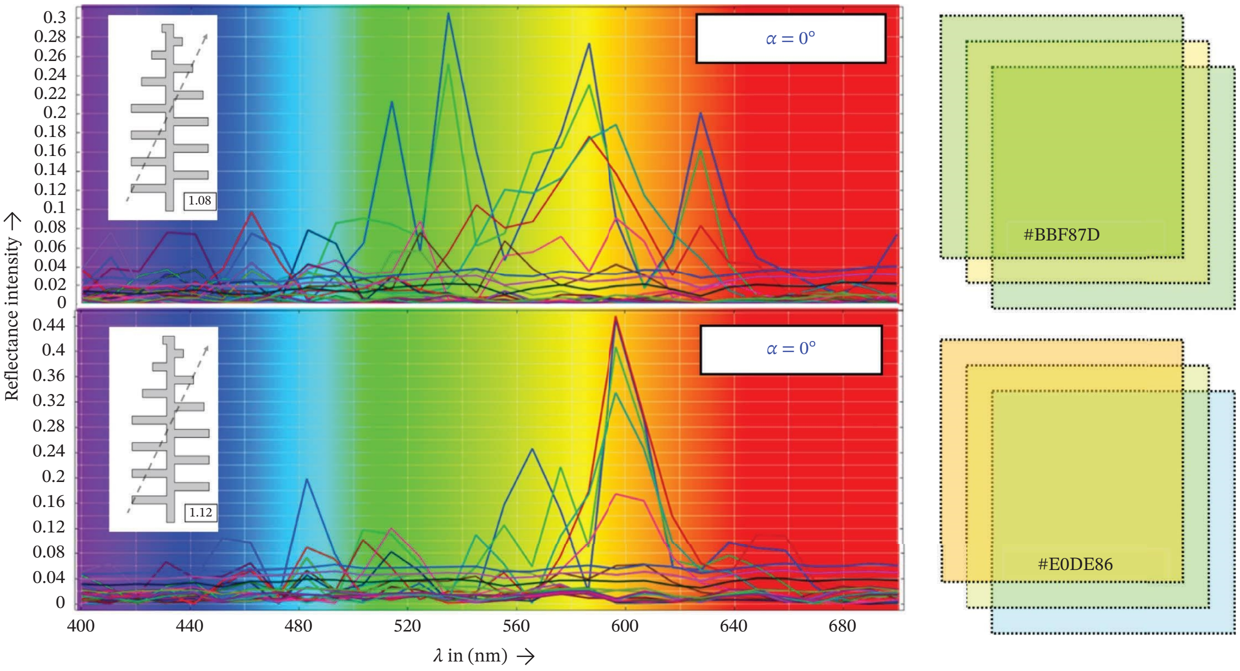

FIGURE 9 | Reflectance spectra and associated effective colours for the incidence angle with the highest reflectance intensity after scaling the structure by 1.08 and 1.12, respectively. Each curve represents a fixed incidence angle, while the dark-blue curves in both plots represent the curve with the highest reflectance intensity.

wavelength decreases. Consequently, blue wavelengths exhibit both sharper and more intense reflectance peaks than longer wavelengths, a behaviour that mirrors the naturally intense iridescence of Morpho butterflies. When the structure is upscaled, the increased periodicity permits higher-order interference modes to contribute more strongly, broadening the spectral response and allowing multiple colour bands to appear simultaneously. This interplay between interference order, optical path length, and wavelength-dependent scattering efficiency gives rise to the structured evolution of colour observed across the full scaling range.

Together, these mechanisms show that the dominant determinant of the reflected colour is the geometry of the surface

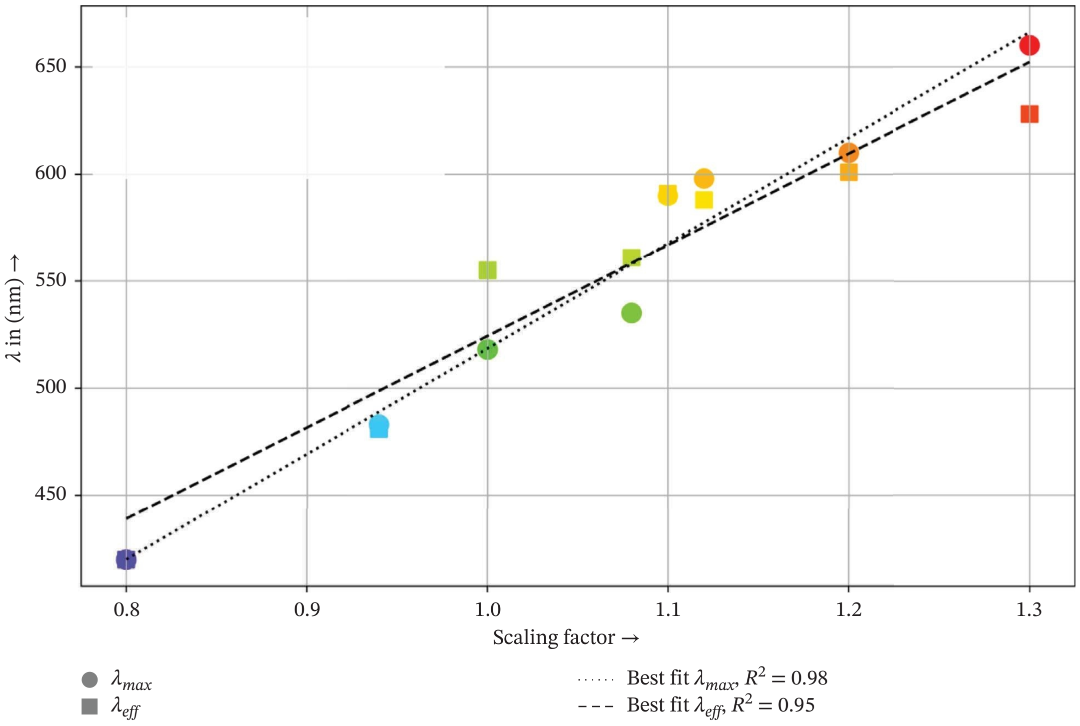

FIGURE 10 | Reflectance spectra at incidence angle 0° for different colours with scaling factors referenced to the green graph from the initial structure (Figure 2(a)).

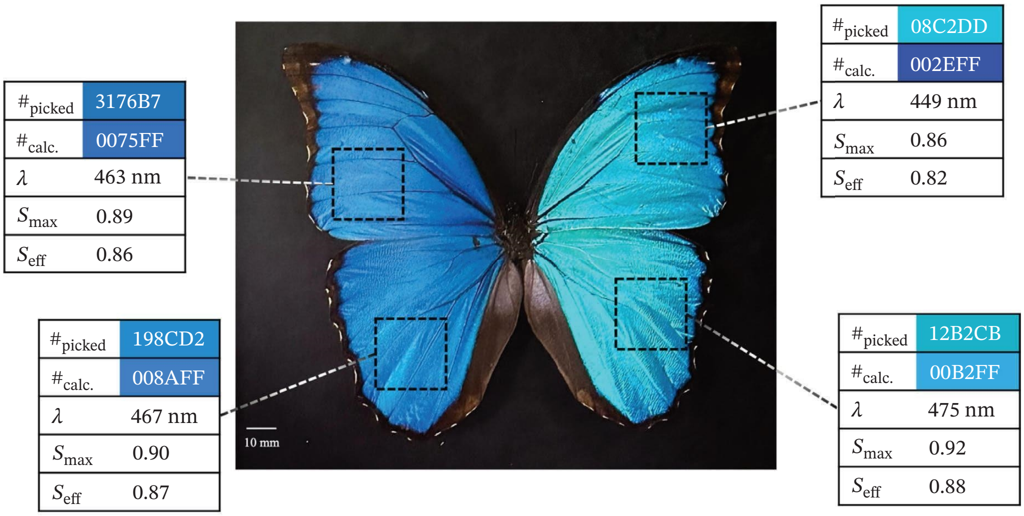

$\#_{\text{picked}}$	3176B7
$\#_{\text{calc.}}$	0075FF
λ	463 nm
$S_{\max}$	0.89
S_{eff}	0.86

$\#_{\text{picked}}$	08C2DD
$\#_{\text{calc.}}$	002EFF
λ	449 nm
$S_{\max}$	0.86
S_{eff}	0.82

$\#_{\text{picked}}$	198CD2
$\#_{\text{calc.}}$	008AFF
λ	467 nm
$S_{\max}$	0.90
S_{eff}	0.87

$\#_{\text{picked}}$	12B2CB
$\#_{\text{calc.}}$	00B2FF
λ	475 nm
$S_{\max}$	0.92
S_{eff}	0.88

FIGURE 11 | Visualising the closeness between the actual and predicted colours in different sections of the *Morpho didius* wing. Thereby, the colour shimmering in the image is attributed to different incidence angles. While λ was calculated using the function for identifying the "closest" wavelength for a given HEX colour code (Figure 5), $S_{\max}$ and S_{eff}, referring to "Scaling with $\lambda_{\max}$ peak" and "Scaling with λ_{eff} peak" were calculated using the derived predictive models.

nanostructure, while material-specific optical constants primarily influence the absolute spectral position. Because geometric rescaling alone can compensate for those material differences, as demonstrated by the 6% downscaling that recovers the reference blue reflectance, structural design emerges as a robust, material-agnostic route for engineering and transferring structural colours across different dielectric platforms. Thus, within a greater picture, these findings position the present scaling framework as a complementary design tool to recent photonic crystal and bioinspired photonic architecture approaches, while current state-of-the-art photonic systems increasingly exploit complex three-dimensional periodicity and hierarchical design to achieve programmable and multifunctional optical responses [5–7]. The results show that potentially a single or few global rescaling parameters can recover comparable target colours even under material substitution, as demonstrated by the 6% downscaling that mitigates the material-induced spectral offset between SiC and biologically derived reference systems. Therefore, the presented framework provides a compact and fabrication-tolerant design rule that can be used to rapidly target desired wavelengths prior to photonic crystal optimization and helping to transfer a given colour response between different material platforms and reducing effort in redesigning the architectural motif [8].

4 | Conclusions

This study demonstrates that structural colour can be predictably engineered through controlled geometric scaling of morpho-inspired photonic nanostructures, independent of the underlying material platform. Using electromagnetic finite-element simulations, we quantified how uniform scaling drives systematic spectral shifts: a 6% reduction in feature size shifts the peak reflectance from 503 nm (turquoise-green) to 482.7 nm (blue), nearly doubling the peak reflectance to ≈0.6 compared with the original geometry. Conversely, scaling the structure by 8% and 12% shifts the reflectance maximum into the green-yellow (547 nm) and orange (598 nm) regions, accompanied by increased spectral bandwidth and a reflectance gain of 0.142 relative to the baseline configuration. Across the full scaling range, the relationship between geometry and optical response follows a robust linear trend ($R^2 > 0.95$ for both λ_{max} and λ_{eff}), enabling both forward design, predicting the colour produced by a given structure and inverse specification, identifying the required geometry for a target colour. Crucially, we show that geometric rescaling alone can compensate for differences in material refractive index: despite using SiC rather than biologically accurate chitin, a simple 6% rescaling reproduces the experimentally validated blue reflectance reported by Siddique et al. This confirms that surface geometry, rather than material composition, is the dominant determinant of structural colour, establishing a *material-agnostic design rule* for colour tuning. Angle-resolved simulations further reveal that maximum reflectance consistently occurs at shallow incidence angles, reflecting enhanced constructive interference and surface-confined light transport. The present model intentionally isolates a periodic morpho-inspired unit cell to extract geometry-driven design rules for structural colour. While extended surfaces in natural and engineered systems exhibit inter-ridge disorder, finite-size effects, and coherence loss at larger length scales, these factors primarily affect angular diffusion and spectral bandwidth rather than the central wavelength of the dominant reflectance peak. The linear scaling relationship identified here is governed by local optical path length and phase-matching conditions within the lamellar geometry and is therefore expected to remain valid when multiple units are assembled, provided the local structural motif is preserved. Incorporating multi-unit interactions, controlled disorder, and defect-induced scattering represents an important direction for future work but does not alter the geometry-dominated wavelength–scaling principle established in this study. Together, these results show that structural colour can be rationally programmed through nanoscale geometry, offering a compact predictive framework for designing photonic surfaces with tunable optical responses. The ability to recover target structural colours across different material platforms through geometric rescaling alone establishes a practical and material-transferable design rule, addressing a key bottleneck in predictive structural colour modelling.

Author Contributions

The following contributions are based on the Contributor Roles Taxonomy (CRediT): conceptualization, Tobias Rosnitschek; methodology, Sara Al-Motori and Tobias Rosnitschek; software, Sara Al-Motori; validation, Tobias Rosnitschek and Christian Orgeldinger; formal analysis, Tobias Rosnitschek and Sara Al-Motori; investigation, Sara Al-Motori, Tobias Rosnitschek and Christian Orgeldinger; resources, Markus Zimmermann and Stephan Tremmel; data curation, Tobias Rosnitschek; writing–original draft preparation, Sara Al-Motori and Christian Orgeldinger; writing–review and editing, Tobias Rosnitschek, Markus Zimmermann, and Stephan Tremmel; visualization, Sara Al-Motori and Tobias Rosnitschek.

Acknowledgements

The authors greatly acknowledge the continuous support of the University of Bayreuth.

Funding

This research received no external funding.

Disclosure

All authors have read and agreed to the published version of the manuscript.

Conflicts of Interest

The authors declare no conflicts of interest.

Data Availability Statement

The data that support the findings of this study are openly available in Zenodo at https://doi.org/10.5281/zenodo.15671959.

References

1. R. H. Siddique, S. Diewald, J. Leuthold, and H. Hölscher, "Theoretical and Experimental Analysis of the Structural Pattern Responsible for the Iridescence of Morpho Butterflies," *Optics Express* 21, no. 12 (2013): 14351, https://doi.org/10.1364/OE.21.014351.

2. C. P. Barrera-Patiño, J. D. Vollet-Filho, R. G. Teixeira-Rosa, et al., "Photonic Effects in Natural Nanostructures on Morpho Cypris and Greta Oto Butterfly Wings," *Scientific Reports* 10 (2020): 5786, https://doi.org/10.1038/s41598-020-62770-w.

3. B. Song, V. E. Johansen, O. Sigmund, and J. H. Shin, "Reproducing the Hierarchy of Disorder for Morpho-Inspired, Broad-Angle Color Reflection," *Scientific Reports* 7, no. 1 (2017): 46023, https://doi.org/10.1038/srep46023.

4. G. Zyla and M. Farsari, "Frontiers of Laser-Based 3D Printing: A Perspective on Multi-Photon Lithography," *Laser & Photonics Reviews* 18, no. 7 (2024): 2301312, https://doi.org/10.1002/lpor.202301312.

5. Y. Cho, H. H. Kim, S. Ahn, et al., "Colloidal Opaline Composites as Throughput-Scalable, Fully Transparent, and Color-Tunable Radiative Cooling Exterior Films for Outdoor Photovoltaics," *Advanced Functional Materials* 35, no. 52 (2025): e10833, https://doi.org/10.1002/adfm.202510833.

6. Y. Cho, S. H. Park, M. Kwon, H. H. Kim, J. Huh, and S. Lee, "Van der Waals Colloidal Crystals," *Advanced Materials* 36, no. 23 (2024): 2312748, https://doi.org/10.1002/adma.202312748.

7. G. Posnjak, X. Yin, P. Butler, et al., "Diamond-Lattice Photonic Crystals Assembled From DNA Origami," *Science* 384, no. 6697 (2024): 781–785, https://doi.org/10.1126/science.adl2733.

8. M. Kolle and S. Lee, "Progress and Opportunities in Soft Photonics and Biologically Inspired Optics," *Advanced Materials* 30, no. 2 (2018): 1702669, https://doi.org/10.1002/adma.201702669.

9. T. J. Cui, D. R. Smith, and R. Liu, *Metamaterials: Theory, Design, and Applications* (Springer, 2010).

10. V. Kaushik, "Metamaterials" (2019), https://doi.org/10.13140/RG.2.2.28478.64322.

11. J. Valentine, S. Zhang, T. Zentgraf, et al., "Three-Dimensional Optical Metamaterial With a Negative Refractive Index," *Nature* 455, no. 7211 (2008): 376–379, https://doi.org/10.1038/nature07247.

12. W. Cai and V. Shalaev, *Optical Metamaterials* (Springer, 2010), https://doi.org/10.1007/978-1-4419-1151-3.

13. X. Zhao, Y. Xiong, W. Wang, W. Zhang, and D. Zhang, "Achieving Structural White Inspired by Quasiordered Microstructures in Morpho Theseus," *NPG Asia Materials* 15, no. 1 (2023): 20, https://doi.org/10.1038/s41427-023-00463-2.

14. J. Teyssier, S. V. Saenko, D. Van Der Marel, and M. C. Milinkovitch, "Photonic Crystals Cause Active Colour Change in Chameleons," *Nature Communications* 6, no. 1 (2015): 6368, https://doi.org/10.1038/ncomms7368.

15. E. R. Dufresne, H. Noh, V. Saranathan, S. G. J. Mochrie, H. Cao, and R. O. Prum, "Self-Assembly of Amorphous Biophotonic Nanostructures by Phase Separation," *Soft Matter* 5, no. 9 (2009): 1792, https://doi.org/10.1039/b902775k.

16. M. D. Shawkey, V. Saranathan, H. Pálsdóttir, et al., "Electron Tomography, Three-Dimensional Fourier Analysis and Colour Prediction of a Three-Dimensional Amorphous Biophotonic Nanostructure," *Journal of the Royal Society Interface* 6 (2009): https://doi.org/10.1098/rsif.2008.0374.focus.

17. M. D. Shawkey, N. I. Morehouse, and P. Vukusic, "A Protean Palette: Colour Materials and Mixing in Birds and Butterflies," *Journal of the Royal Society Interface* 6, no. suppl_2 (2009): https://doi.org/10.1098/rsif.2008.0459.focus.

18. S. Kinoshita, S. Yoshioka, and J. Miyazaki, "Physics of Structural Colors," *Reports on Progress in Physics* 71, no. 7 (2008): 076401, https://doi.org/10.1088/0034-4885/71/7/076401.

19. A. E. Seago, P. Brady, J.-P. Vigneron, and T. D. Schultz, "Gold Bugs and Beyond: A Review of Iridescence and Structural Colour Mechanisms in Beetles (Coleoptera)," *Journal of the Royal Society Interface* 6, no. suppl_2 (2009): https://doi.org/10.1098/rsif.2008.0354.focus.

20. S. Yoshioka, S. Kinoshita, H. Iida, and T. Hariyama, "Phase-Adjusting Layers in the Multilayer Reflector of a Jewel Beetle," *Journal of the Physical Society of Japan* 81, no. 5 (2012): 054801, https://doi.org/10.1143/JPSJ.81.054801.

21. A. Didari and M. P. Mengüç, "A Biomimicry Design for Nanoscale Radiative Cooling Applications Inspired by *Morpho didius* Butterfly," *Scientific Reports* 8, no. 1 (2018): 16891, https://doi.org/10.1038/s41598-018-35082-3.

22. A. Saito, "Material Design and Structural Color Inspired by Biomimetic Approach," *Science and Technology of Advanced Materials* 12, no. 6 (2011): 064709, https://doi.org/10.1088/1468-6996/12/6/064709.

23. T. Rosnitschek and S. Al-Motori, "Simulation Model for the Structural Color in *Morpho didius* Wings" (2025), https://doi.org/10.5281/ZENODO.15671959.

24. Z. C. Feng, ed., in *SiC Power Materials: Devices and Applications*, 73 (Springer, 2004).

25. K. K. Sharma, *Optics: Principles and Applications* (Elsevier Science & Technology, 2006).

26. M. Gmelch and S. Reineke, in *Durchblick in Optik: mit Phänomenen, Formeln und Fragen zum Verständnis* (Springer, 2019).

27. W. Nolting, in *Grundkurs Theoretische Physik 3: Elektrodynamik* (Springer, 2013).

28. B. Krüger, T. Brenner, and A. Kienle, "Solution of the Inhomogeneous Maxwell's Equations Using a Born Series," *Optics Express* 25 (2017): 25165, https://doi.org/10.1364/OE.25.025165.

29. E. Silaeva, L. Saddier, and J.-P. Colombier, "Drude-Lorentz Model for Optical Properties of Photoexcited Transition Metals Under Electron-Phonon Nonequilibrium," *Applied Sciences* 11, no. 21 (2021): 9902, https://doi.org/10.3390/app11219902.

30. W. Shi, D. E. S. Koo, M. Kitano, et al., "Pre-Processing Visualization of Hyperspectral Fluorescent Data With Spectrally Encoded Enhanced Representations," *Nature Communications* 11, no. 1 (2020): 726, https://doi.org/10.1038/s41467-020-14486-8.

31. D. Carreres-Prieto, J. T. García, F. Cerdán-Cartagena, and J. Suardiaz-Muro, "Performing Calibration of Transmittance by Single RGB-LED Within the Visible Spectrum," *Sensors* 20, no. 12 (2020): 3492, https://doi.org/10.3390/s20123492.